Lui, H., Stolle, C., Förster, M., Watanabe, S. (2007): Solar activity dependence of the electron density at 400 km at equatorial and low latitudes observed by CHAMP. - Journal of Geophysical Research, 112, A11311,

DOI: 10.1029/2007JA012616

Solar activity dependence of the electron density at 400 km at equatorial and low latitudes observed by CHAMP

Huixin Liu

Earth and Planetary Science Division, Hokkaido University, Sapporo, Japan.

Claudia Stolle

GeoForschungsZentrum Potsdam, Potsdam, Germany

Matthias Förster

GeoForschungsZentrum Potsdam, Potsdam, Germany

Shigeto Watanabe

Earth and Planetary Science Division, Hokkaido University, Sapporo, Japan

H. Liu, S. Watanabe, Earth and Planetary Science Division, Hokkaido University, Sapporo 060-0810, Japan. (huixin@ep.sci.hokudai.ac.jp)

C. Stolle and M. Förster, GeoForschungsZentrum Potsdam, D-14473 Potsdam, Germany

Abstract.

We have investigated the solar activity dependence of the electron density at equatorial and low latitudes using six years of measurements between Aug. 1, 2000–Aug. 1, 2006 from the CHAMP satellite, and compared it with the International Reference Ionosphere model (IRI). The solar activity dependence observed by CHAMP at 400 km altitude exhibits significant variation with latitude, season and local time. First, the electron density in the crest regions of the Equatorial Ionization Anomaly (EIA) grows roughly linearly from solar minimum to solar maximum, with higher growth rate than that in the EIA trough region. Second, the solar activity dependence in the EIA crest regions varies strongly with season. The growth rate of the electron density with increasing solar activity around equinoxes is about 1.5 to 2 times of that near solstices. Third, the solar activity dependence of the EIA structure varies significantly with local time. In the noon sector, the crest-to-trough ratio (CTR) obtained at 400 km altitude varies within only a small range between 1.14 and 1.43 from solar minimum to solar maximum. In the post-sunset local time sector, however, the CTR grows remarkably with solar activity level, reaching values of above 3.9 at solar maximum. These differences are attributed to the different solar activity dependence of the vertical plasma drift in corresponding local time sectors. The IRI model was found to reproduce well the equatorial electron density near 400 km in the noon sector at all solar activity levels. However, it significantly overestimates it in the post-sunset to pre-midnight sector at high solar activity levels. The major

cause for this overestimation has been found to be the IRI's inadequate representation of the F2 layer maximum height (hmF2) in this sector, while the IRI's lack of equatorial spread F seems to play only a very small role.

1. Introduction

The Earth's ionosphere is mainly formed via photo-ionization of the upper atmosphere by solar EUV and X-ray radiation. Since the solar radiation changes significantly at various time scales, the ionosphere tends to undergo similar variations. Among these, solar cycle is an important long-term variation [e.g. *Bilitza and Hoegy*, 1990; *Balan et al.*, 1994a; *Truhlík et al.*, 2003]. A number of ionospheric quantities have been found to be solar cycle dependent, for instance, the maximum F-region electron density (NmF2) and the related critical frequency (foF2), the total electron content, etc [see e.g. *Balan et al.*, 1994b; *Bilitza and Williamson*, 2000; *Liu et al.*, 2006, 2007b]. In addition to solar radiation, the state of the neutral atmosphere and ionospheric electrodynamics strongly influence various ionospheric properties as well. Particularly in tropical regions (including equatorial and low latitudes), the ionospheric structure is dominantly controlled by the so-called fountain process, which is driven by the large-scale eastward electric field via $\vec{E} \times \vec{B}$ drift [e.g. see *Rishbeth*, 2000, and references therein]. It forms the well-known EIA structure, with an electron density trough at the dip equator sandwiched by two high density bands off the dip equator. This unique electrodynamic process related to the equatorial fountain is expected to play an important role in the solar activity dependence of the F-region ionosphere in tropical regions, and to distinguish the EIA trough from crest regions. This forms the principle motivation of our study.

Another purpose of this study is to evaluate the IRI model in tropical regions. The IRI is an important empirical climatological model of the Earth's ionosphere and has been continuously updated [*Bilitza*, 1992, 2003]. The model version IRI-2001 has included a large collection of ground and satellite observations and is expected to give a reasonably description of the ionosphere under quiet geomagnetic conditions. However, there are evidences showing the need for further improvement in specific regions. Particularly in the post-sunset equatorial and low latitudes, key ionospheric parameters like the maximum density of the F2 region electron density and height (NmF2 and hmF2) often deviate significantly from observations [e.g. *Adeniyi et al.*, 2003; *Obrou et al.*, 2003; *Souza et al.*, 2003; *Abdu et al.*, 2004]. This strongly affects the IRI's predictions of the electron density in terms of either height profile or absolute values at certain altitude in this local time sector [*Uemoto et al.*, 2007; *Liu et al.*, 2007a]. On the other hand, this region is an interesting and important part of the ionosphere, where the combination of the zonal wind and the local time/longitude gradient of the field-aligned integrated E-region conductivity across the evening terminator causes the development of the pre-reversal enhancement (PRE) [see e.g. *Kelley*, 1989]. This subsequently raises the ionosphere to higher altitude, which promotes the generation of the equatorial spread F (ESF) [*Tsunoda*, 1985] and the formation of the fast neutral wind channel [*Raghavarao et al.*, 1991], which are important phenomena in equatorial regions. Therefore, it is highly desirable to have a more reliable IRI representation of this region for various theoretical and practical purposes. In present study, we focus on the tropical region and carry out a model-data comparison for various solar flux levels. By doing so, we attempt to characterize systematic differences between the IRI predicted electron density with those observed by the CHAMP satellite, hence to provide useful information for its improvement.

2. Data selection and analysis

The CHAMP (CHAllenging Minisatellite Payload) satellite was launched on 15 July 2000 into a near-circular orbit with an inclination of $87.3°$ and an initial nominal altitude of 456 km. Its orbital plane precesses through all local times every four months and through all longitudes at a fixed local time every 24 hours. The CHAMP measures the in-situ ion density (assumed to be O^+) using a Planar Langmuir Probe (PLP) every 15 s. The Ne retrieving procedure is described in *McNamara et al.* [2007] along with a validation of the Ne measurements. By comparing with the plasma frequency measurements of the Jicamarca digisonde, they found the mean discrepancy between the PLP and the ionosonde records to be 4% and 2.6% for CHAMP orbital heights below and above the F2 peak, respectively. Readers are kindly referred to *McNamara et al.* [2007] for detailed procedures regarding this comparison.

Our analysis of the solar activity dependence of the electron density is based on the PLP data from Aug. 1, 2000 to Aug. 1, 2006. IRI-2001 Model (marked as IRI in the following) predictions were generated for every sample point of the measurements. Only data under quiet geomagnetic conditions (Kp≤3+) are used to limit effects from geomagnetic disturbance. Furthermore, since the CHAMP orbit has decayed from 456 km height to about 350 km during these six years, a normalization of the data to a common altitude of 400 km has been applied to possibly exclude variations induced by the orbit decay. The normalization is done as: $CHAMP(400km) = CHAMP(h)\frac{IRI(400km)}{IRI(h)}$, where h denotes CHAMP's orbital height (h). Although this procedure may introduce some uncertainties from the model to the data, for the analysis of the solar activity dependence, it is highly necessary to avoid density variations due to the large altitude changes.

In this study, we have chosen the proxy $P = (F10.7 + F10.7A)/2$ to represent the solar activity. Here F10.7A is the 81-day average of the F10.7 values centered on the day of interest. Previous studies [e.g. *Richards et al.*, 1994; *Liu et al.*, 2006] have shown that this proxy is more suitable than F10.7 as a linear indicator for the Solar EUV radiations. The variation of the F10.7 and P during the period of Aug. 1, 2000 – Aug. 1, 2006 are shown in Figure 1. **Figure 1**

Due to the smoothing behavior of P the range of the solar flux variation becomes smaller when using P instead of F10.7 as the proxy. We have repeated the following analysis with both P and F10.7, and found that using P gives a significantly higher correlation when the solar activity dependence is studied quantitatively like those shown later in Figures 7 and 8. But it makes little difference for qualitative analysis which uses only rough grouping of the solar activity, like that discussed for Figures 2 and 6 in the following sections.

3. Results

In this section, after examining the solar activity dependence of the diurnal variations at the dip equator, we expand in latitudes to investigate the EIA structure and its solar activity dependence. In particular, we focus on the differences between the EIA crest and trough regions, and also on the differences between the noon and post-sunset local time sectors.

3.1. Solar activity dependence of the diurnal variation at the dip equator

We have compared the diurnal variation of the electron density obtained from CHAMP within $\pm 5°$ dip latitudes with that modeled by IRI at three different solar activity levels, low for $P < 100$, moderate for $100 \leq P \leq 150$, and high for $150 < P < 200$. Since saturation occurs for P above 200 as shown by several studies [*Balan et al.*, 1994b; *Liu et al.*, 2006] and also will be seen in section 3.2.2, data points at $P \geq 200$ are not used in this section. It should be noted that the diurnal variations presented here are longitudinally averaged.

We see in Figure 2 that at low and moderate solar activity levels, the Ne diurnal variation generally consists of a dayside maximum, whose local time varies around 14 LT depending on season. However, the maximum at 18 LT near Sept. equinox at low solar flux level appears to be different from that shown in all other cases in Figure 2. At the moment, we cannot explain this **Figure 2** single deviating behavior. After reaching the maximum, the density then decays monotonically till dawn, forming a minimum at about 05 LT. At high solar activity levels, however, the post-sunset decay is dramatically intensified in all seasons. The density rapidly drops to a minimum near 20 LT, then increases again towards midnight. This feature, combined with the density decay after midnight, results in a midnight density maximum which is not discernible at low and moderate solar activity levels. In comparison, the IRI model reproduces pretty well the observed diurnal variation at low and moderate solar activity levels at all local times. However, a striking CHAMP-IRI discrepancy stands out in the post-sunset period at high solar flux levels. It reaches nearly 100% near March equinox and above $\sim$50% in other seasons. Consequently, the IRI is unable to capture the midnight density maximum seen by CHAMP.

The post-sunset period is a region experiencing extreme electrodynamic processes and also frequent occurrence of the ESF. If CHAMP happens to be sampling through ESFs, which are characterized by large density depletion, it would then tend to give a lower average Ne than the IRI predictions (the IRI does not include ESF signatures). To investigate the possibility of such ESF influences, we examined the longitudinal distribution of the CHAMP-IRI difference between 19–23 LT at high solar activity levels. Results are shown in Figure 3. Figure 4 presents the ESF occurrence rate in corresponding seasons as detected from CHAMP's total magnetic field measurements, which represents a linear measure of the related electron density gradients [*Stolle et al.*, 2006]. Comparing these two figures, we notice the following features. The longitudinal distribution of the CHAMP-IRI difference seems to somehow follow that of the ESF. For instance, the difference maximizes near $290°$ around December solstice, and near $20°$ and $150°$ around June solstice. These longitudinal sectors coincident with those of frequent ESF occurrences, hence indicating possible ESF contribution to the lower average Ne values from

Figure 3

Figure 4

CHAMP. However, this figure also shows evidences that the ESF is not the principle contributor to the CHAMP-IRI discrepancy. This is because, first, the CHAMP Ne values are significantly ($\sim 20\%$) below the IRI values at all longitudes, even in regions where almost no ESF occurs. Second, the CHAMP-IRI difference exhibits a clear seasonal variation, being largest near March equinox. This cannot be explained by the seasonal variation of the ESF occurrence rate. Take the longitude sector near $180°$ for example, the CHAMP-IRI difference near March equinox reaches value of ~90%, which is nearly double of that around June solstice. However, the ESF occurrence rate near March equinox is only about half of that around June solstice. Therefore, there must be a more principle cause for the CHAMP-IRI discrepancy.

This principle cause is likely to be the IRI's inadequate representation of the F2 peak height in post-sunset periods [*Bilitza*, 2003; *Adeniyi et al.*, 2003; *Souza et al.*, 2003; *Abdu et al.*, 2004]. It is known that the ionosphere is lifted up considerably after sunset by increasing upward plasma drifts related to the pre-reversal enhancement of the eastward electric field [e.g. *Abdu*, 2001, and references therein]. The degree of uplift positively depends on the pre-reversal enhancement, whose magnitude has been shown by *Fejer et al.* [1995] to increase with solar cycle, particularly near equinox and December solstice. However, the IRI's description of the post-sunset hmF2 at equatorial regions has been shown to fall more than 100 km below the real hmF2 at high solar flux levels [see figures in e.g. *Adeniyi et al.*, 2003; *Obrou et al.*, 2003; *Abdu et al.*, 2004]. In this case, the altitude of 400 km becomes much closer to the IRI-predicted hmF2 than to the real hmF2, leading to the IRI's overestimation of Ne at 400 km. Since the pre-reversal enhancement is stronger near equinoxes and December solstice than near June solstice, the CHAMP-IRI discrepancy can be expected to vary accordingly. And this is exactly what Figure 2 reveals, with larger differences near March equinox and December solstice, and smaller difference near June solstice. This provides strong evidence that the large data-model discrepancy in the post-sunset period is dominantly due to IRI's strong underestimation of the hmF2 at high solar activity levels.

Figure 5 shows several types of Ne profiles seen on CHAMP satellite passes at high solar activity levels. The corresponding IRI predictions are given by the black curves.The satellite tracks are all near 20 LT. The pink and green ones show normal quiet-time EIA profiles, but with ESF signature in the green track. The red curve shows large depletion in the EIA trough regions which often appears during magnetic storms. We can see that the IRI overestimates the equatorial Ne values for all types of profiles, with a shorter distance between the two EIA crests. This strongly suggests the post-sunset F region by IRI is not lifted sufficiently high enough. Superposed on this, ESF can also contribute to the CHAMP-IRI discrepancy to a very small degree. Storm-time passes like the red curve are not included in the current study of quite-time ionospheric features, but is shown here to serve as an example of huge uplift of the F2 layer. In this case, CHAMP tends to sample regions far down to the bottomside of the F2 layer and hence lead to even larger CHAMP-IRI difference. **Figure 5**

3.2. The solar activity dependence of the EIA structure

The variation of the electron density with solar activity is different for different local times, as we have seen in Figure 2. Two local time sectors show particularly strong solar activity dependence. One is the noon time sector, the other is the post-sunset sector. In this section, we take a closer look at how Ne varies with solar activity in these two local time sectors and how this solar activity dependence differs in the EIA trough and crest regions. To emphasize the first-order LT variation, we tried to minimize the effect of longitudinal variations. This is done by taking daily averaged values from CHAMP. Since CHAMP has a full longitudinal coverage during one day, using daily averaged values keeps the longitudinal bias to be negligible in the following figures. Furthermore, daily values are more suitable for quantitative correlation analysis between Ne and P, like the one shown later in Figures 7 and 8. This is because the solar flux indices P or F10.7 are generally available as daily values. Using track by track satellite data which includes all variations with time-scales down to 93 minutes (the orbit period) would inevitably degrade the correlation significantly.

3.2.1. Comparison between the noon and post-sunset local time sectors

Figure 6 presents the EIA latitudinal profiles at four solar activity levels in the noon (11–15 LT) and post-sunset sector (18–23 LT) around equinoxes. A common parameter to characterize the EIA structure is the crest-to-trough ratio (CTR). Similar to that given in *Mendillo et al.* [2000], this parameter is defined here as $CTR = \frac{Ne_{ncrest}+Ne_{screst}}{2Ne_{trough}}$, which are the ratio of the mean of the northern and southern EIA crest peak value to the minimum Ne in the EIA trough. In this way, a CTR value of one indicates there is no discernible EIA structure. Table 1 summarizes the CTR values at different P levels derived from CHAMP electron density curves in Figure 6. This figure also shows that the location of the peak value in the EIA crests tends to move poleward with increasing solar activity. This trend is stronger in the post-sunset sector than in the noon sector.

Figure 6

We now compare the EIA variation in the noon and post-sunset local time sectors. At noon, the CTR varies within a small range from 1.14 for low P levels to 1.43 for very high P levels. This reflects the fact that the noon-time EIA profiles tend to be lifted up as a whole, but with little change in shape as seen in Figure 6. In addition, the blue curve is falling nearly on top of the red one, indicating a trend of saturation for P above 200 in tropical regions. After sunset, the CTR slightly increases from 1.30 to 1.47 from low to moderate P levels. But it jumps to

3.9 at high P levels. The nearly 3 times enhancement of the CTR value is mainly caused by large rise of Ne values in the EIA crest regions. The trough region Ne stays nearly the same as that for moderate P levels. The resulted large CTR value is accompanied by an apparent poleward movement of the EIA crests from about $\pm 10^{\circ}$ at moderate P levels to about $\pm 15^{\circ}$ at high P levels. For very high solar activity levels with $P > 200$, the crest Ne tends to show little increase, whereas the trough Ne decreases to values far below that for low P levels. This leads to an extremely high CTR value of 29.17. Therefore, the post-sunset EIA structure and the related electron density exhibits a much stronger solar activity dependence than those around noon.

The cause for the depletion of the post-sunset trough region at P above 150 is possibly related to the relative location of the observational altitude (400 km) to hmF2 at different solar activity levels. As mentioned in section 3.1, the ionosphere is lifted to higher altitude due to the pre-reversal enhancement near the evening terminator. The degree of the uplifting increases with increasing solar activity. Thus, the altitude of 400 km may possibly be above hmF2 at low solar activity levels (P$<$150) but below it at high solar activity levels (P$>$150). We have done a rough calculation with the vertical drift model of *Scherliess and Fejer* [1999] to estimate the uplift effect. We found that the large equatorial depletion shown in the blue curve of Figure 6 can be sufficiently produced by pre-reversal enhancements with peak upward drift of about 50 – 60 m s^{-1} at high solar flux levels. The resulting uplift of the F-layer can reach 150–200 km within the time span of the pre-reversal enhancement (which commences after the local sunset at ionospheric heights and continues till the westward turning of the zonal electric field). This would most probably lift the hmF2 to altitudes above 500 km like those observed by *Abdu et al.* [2004]. The dropping of the observational height relative to hmF2 would potentially lead to a stronger decrease of Ne at the dip equator, hence a larger CTR than the one that would be obtained from the NmF2. This makes it somewhat complicated to quantitatively relate the CTR variation from CHAMP at a fixed altitude to the vertical plasma drift. However, it does demonstrate the extremely dynamic nature of the post-sunset ionosphere.

In comparison to CHAMP measurements, IRI reproduces the noon time EIA structure reasonably well, though some overestimation of Ne at both high and low P levels can be noticed. In the post-sunset sector, the model deviates largely from the observations. In particularly, it strongly overestimates the trough region Ne for P above 150, which is consistent with that shown in the right column of Figure 2. Underestimation of the crest region Ne occurs at all solar activity levels with P over 100. In addition, the EIA crests locate about 5° equatorward than the observed ones. These discrepancies strongly suggest an IRI underestimation of the hmF2 at the equator in the post-sunset period.

3.2.2. The Ne-P correlation

Scatter plots of Ne over P in the EIA trough and crest regions are shown in Figure 7 and Figure 8 for noon and post-sunset local time sectors, respectively. The significance of the solar activity dependence can be represented by the slopes of the fitted lines and has been summarized in Figure 9.

Figure 7 **Figure 8** **Figure 9**

The noon sector exhibits several noticeable features. First, regardless of trough or crest region, a significantly positive correlation prevails for solar activity levels with P$<$200. Saturation tends to occur for P above 200, as can be seen in Figure 7 around September equinox and December solstice, where data are available. Due to this reason, the slopes have been calculated without data samples at $P > 200$ for all cases in Figures 7 and 8. Second, the solar activity dependence is apparently stronger in the EIA crest regions than in the trough region as shown in Figure 9. Third, the solar activity dependence in the EIA crest regions varies with season. It is highest around March equinox and lowest near June solstice. This contrasts strongly with the EIA trough region, where little seasonal variation is observed.

In the post-sunset period, the solar activity dependence of the EIA crest Ne experiences a clear seasonal variation, being strong around equinoxes and weak around June solstices. Furthermore, unlike the equinox asymmetry at noon, the post-sunset EIA crest regions exhibits similar values for the slopes near March and September equinox, resulting in prominent semi-annual variation of the solar activity dependence. The values of the slopes are generally larger than those at noon in corresponding seasons. In the EIA trough region after sunset, however, Ne is nearly uncorrelated with the solar flux, as indicated by the low ”R” values in Figure 8. Detailed examination shows that the equatorial Ne tends to slightly increase with P at solar flux levels with $P<150$, while decreases rapidly with P for $P>150$ around March equinox for instance. This is consistent with the post-sunset EIA behavior in the trough region presented in Figure 6, where the trough Ne value increases first then depletes at P above 150.

4. Discussion

We have investigated the solar activity dependence of electron density at an altitude of 400 km obtained from the CHAMP satellite observations. Significant variations with latitude, season and local time have been identified.

First, the solar activity dependence varies with latitudes. It is stronger in the EIA crest regions than in trough regions. This is consistent with the trend found by *Liu et al.* [2006] in NmF2 and by *Huang and Cheng* [1995] in TEC. Though explicit explanation was not given in their studies, we think it is likely to be related to the dynamical effect of the equatorial fountain driven by the $\vec{E} \times \vec{B}$ drift. Under the influence of the equatorial fountain, the plasma drifts upward at the dip equator, then falls down to off-equator latitudes and forms the EIA structure. This process tends to remove Ne from the dip equator, and deposit it to the crest regions. When superposed on the enhanced photo-ionization with increasing solar activity levels, it results in a stronger Ne enhancement with P in the crest region than in the trough region on the dayside. In post-sunset periods, the strengthening of the fountain process together with the lack of photo-ionization evidently lead to even larger difference between the solar activity dependence in the crest and trough regions, as seen in Figure 9.

Second, the solar activity dependence of Ne in the EIA crest regions varies significantly with season. It is stronger around equinoxes than solstices as seen in Figure 9. In the post-sunset period, the seasonal variation finds good agreement with the results of *Whalen* [2004]. The author found that NmF2 measured in the EIA crest region at 21 LT grows roughly linearly with the solar activity, but with clearly higher growth rates near equinoxes than near December solstice, and higher growth rates near December solstice than near June solstice. The cause for this has been demonstrated by Whalen to be the $\vec{E} \times \vec{B}$ vertical drift. The vertical drift at the dip equator exhibits linear relation to the solar activity in all seasons, but the linear function has been shown to vary from season to season. The slope of the function is found to be largest around equinoxes and smallest near June solstice. Therefore, the seasonal variation of Ne's solar activity dependence in the post-sunset period can be attributed to that of the $\vec{E} \times \vec{B}$ vertical drift. In the noon sector, our results are consistent with that of *Liu et al.* [2006], who studied the solar activity dependence of the dayside NmF2. They found stronger solar activity dependence around equinox than solstices. Furthermore, they noticed an equinox asymmetry, with stronger dependence near March equinox than near September equinox. Since the dayside vertical drift varies little with solar activity levels, this equinox asymmetry should be caused by other factors. An important one is the solar activity dependence of the neutral density. In Figure 10, we have **Figure 10** examined the neutral mass density simultaneously obtained from the CHAMP satellite at 400 km altitude [*Liu et al.*, 2005]. Since atomic [O] dominates near 400 km, these variations can roughly represent that of [O]. Evidently, the solar activity dependence of [O] is about 60% stronger around March equinox than around September equinox. This difference is sufficient to account for the higher solar activity dependence of the Ne near March equinox.

Furthermore, the solar activity dependence of the EIA varies with local time. Strongest contrast is seen between the noon and post-sunset local time sector. At noon, the crest-to-trough ratio obtained at 400 km altitude varies within only a small range between 1.14 to 1.43 from solar minimum to solar maximum. After sunset, however, it grows remarkably larger at high P level, reaching values of 3.90 and 29.17 at 400 km altitude. This is accompanied with poleward movement of the EIA crests and a depletion of the trough as seen for P$>$150. Since the EIA is directly driven by the vertical drift of the plasma at the dip equator, this difference may be viewed in light of the climatology of the vertical plasma drift. Based on AE-E satellite observations, Fejer et al. (1995) found that the F-region vertical plasma drift is nearly independent of solar activity at daytime, but enhances considerably with solar activity after sunset. Therefore, extra photo-ionization with increasing solar activity combined with a nearly constant vertical transport seems to have led to the increase of Ne at the noon-time dip equator at 400 km altitude. In the post-sunset sector, no photo-ionization exists and the equatorial ionosphere experiences decay via chemical recombination, and upward and poleward transport related to the fountain process. Since the fountain intensifies at high solar flux levels due to enhanced vertical drift, the equatorial Ne near 400 km tends to experience stronger depletion correspondingly. Therefore, CHAMP observations demonstrate the dynamical nature of the post-sunset ionosphere caused by pre-reversal enhancement and its strong solar activity dependence.

Regarding the IRI, we may conclude that it reproduces well the equatorial electron density near 400 km in the noon sector at all solar activity levels. However, it significantly overestimates it in the post-sunset to pre-midnight sector. The CHAMP-IRI comparison indicates that IRI's post-sunset hmF2 at the dip equator falls significantly below the true hmF2, particularly at high solar flux levels. This underestimation seems to be mainly caused by the limited order used for the spherical harmonics representation of M(3000)F2 on which the IRI-hmF2 is based. As pointed out by *Adeniyi et al.* [2003] and *Obrou et al.* [2003], using measured M(3000)F2 values can significantly improve IRI's estimation of hmF2. Furthermore, the possibility of using the correlation between vertical plasma drift and hmF2 to improve the IRI's hmF2 model has also been attempted by *Obrou et al.* [2003].

Acknowledgments. We thank L. Scherliess for providing the vertical drift model code. We also thank H. Lühr for helpful discussions and D. Cooke and Ch. Roth for processing the CHAMP PLP data. The CHAMP mission is supported by the German Aerospace Center (DLR) in operation and by the Federal Ministry of Education and Research (BMBF) in data processing. This work is supported by the Japan Society for the Promotion of Science (JSPS) foundation.

References

Abdu, M. (2001), Outstanding problems in the equatorial ionosphere-thermosphere electrodynamics relevant to spread f, *J. Atmos. Solar-Terr. Phys.*, *63*, 869–884.

Abdu, M. A., I. S. Batista, B. W. Reinisch, and A. J. Carrasco (2004), Equatorial F-layer heights, evening prereversal electric field, and night E-layer density in the American sector: IRI validation with observations, *Advances in Space Research*, *34*, 1953–1965, doi: 10.1016/j.asr.2004.04.011.

Adeniyi, J. O., D. Bilitza, S. M. Radicella, and A. A. Willoughby (2003), Equatorial F2-peak parameters in the IRI model, *Advances in Space Research*, *31*, 507–512.

Balan, N., G. J. Bailey, B. Jenkins, P. B. Rao, and R. J. Moffett (1994a), Variations of ionospheric ionization and related solar fluxes during an intense solar cycle, *J. Geophys. Res.*, *99*, 2243–2253.

Balan, N., G. J. Bailey, and R. J. Moffett (1994b), Modeling studies of ionospheric variations during an intense solar cycle, *J. Geophys. Res.*, *99*, 17,467–17,475.

Bilitza, D. (1992), International reference ionosphere (1990), *Planet. Space Sci.*, *40*, 544–544, doi:10.1016/0032-0633(92)90174-M.

Bilitza, D. (2003), International reference ionosphere 2000: Examples of improvements and new features, *Adv. Space Res.*, *31*, 757–767.

Bilitza, D., and W. R. Hoegy (1990), Solar activity variation of ionospheric plasma temperatures, *Advances in Space Research*, *10*, 81–90, doi:10.1016/0273-1177(90)90190-B.

Bilitza, D., and R. Williamson (2000), Towards a Better Representation of the IRI Topside Based on ISIS and Alouette Data, *Advances in Space Research*, *25*, 149–152.

Fejer, B. G., E. R. de Paula, R. A. Heelis, and W. B. Hanson (1995), Global equatorial ionospheric vertical plasma drifts measured by the AE-E satellite, *J. Geophys. Res.*, *100*, 5769–5776.

Huang, Y.-N., and M. Cheng (1995), Solar cylcle variation of the total electron content around equatorial anomaly crest region in east asia, *J. Atmos. Solar-Terr. Phys.*, *57*, 1503–1511.

Kelley, M. C. (1989), *The Earth's Ionosphere*, Academic Press, New York.

Liu, H., H. Lühr, V. Henize, and W. Köhler (2005), Global distribution of the thermospheric total mass density derived from CHAMP, *J. Geophys. Res.*, *110*, A04301, doi:

10.1029/2004JA010741.

Liu, H., C. Stolle, S. Watanabe, T. Abe, M. Rother, and D. L. Cooke (2007a), Evaluation of the IRI model using CHAMP observations in polar and equatorial regions, *Adv. Space Res.*, doi:10.1016/j.asr.2006.08.006.

Liu, L., W. Wan, B. Ning, O. M. Pirog, and V. I. Kurkin (2006), Solar activity variations of the ionospheric peak electron density, *J. Geophys. Res.*, A08304, doi:10.1029/2006JA011598.

Liu, L., W. Wan, X. Yue, B. Zhao, B. Ning, and M.-L. Zhang (2007b), The dependence of plasma density in the topside ionosphere on the solar activity level, *Ann. Geophys.*, *25*, 1337–1343.

McNamara, L., D. L. Cooke, C. E. Valladares, and B. W. Reinisch (2007), Comparison of CHAMP and Digisonde plasma frequencies at Jicamarca, Peru, *Radio Science*, *42*, doi: 10.1029/2006RS003491.

Mendillo, M., L. Bosheng, and J. Aarons (2000), The application of gps observations to equatorial aeronomy, *Radio Science*, *35*, 885–904.

Obrou, O. K., D. Bilitza, J. O. Adeniyi, and S. M. Radicella (2003), Equatorial F2-layer peak height and correlation with vertical ion drift and M(3000)F2, *Advances in Space Research*, *31*, 513–520.

Raghavarao, R., L. E. Wharton, N. W. Spencer, H. G. Mayr, and L. H. Brace (1991), An equatorial temperature and wind anomaly (ETWA), *Geophys. Res. Lett.*, *18*(9), 1193–1196.

Richards, P. G., J. A. Fennelly, and D. G. Torr (1994), EUVAC: A solar EUV flux model for aeronomic calculations, *J. Geophys. Res.*, *99*, 8981–8992.

Rishbeth, H. (2000), The equatorial f-layer: progress and puzzles, *Ann. Geophys.*, *18*, 730–739.

Scherliess, L., and B. G. Fejer (1999), Radar and satellite global equatorial f region vertical drift model, *J. Geophys. Res.*, *104*, 6829–6842.

Souza, J. R., G. J. Bailey, M. A. Abdu, and I. S. Batista (2003), Comparison of low latitude F region peak densities, heights and equatorial EXB drift from IRI with observational data and the Sheffield University plasmasphere ionosphere model, *Advances in Space Research*, *31*, 501–505.

Stolle, C., H. Lühr, M. Rother, and G. Balasis (2006), Magnetic signatures of equatorial spread F as observed by the CHAMP satellite, *Journal of Geophysical Research (Space Physics)*, *111*, doi:10.1029/2005JA011184.

Truhlík, V., L. Třísková, and J. Šmilauer (2003), Response of outer ionosphere electron temperature and density to changes in solar activity, *Advances in Space Research*, *31*, 697–700.

Tsunoda, R. T. (1985), Control of the seasonal and longitudinal occurrence of equatorial scintillations by the longitudinal gradient in integrated E region Pedersen conductivity, *J. Geophys. Res.*, *90*, 447–456.

Uemoto, J., T. Ono, A. Kumamoto, and M. Iizima (2007), Comparison of the IRI 2001 model with electron density profiles observed from topside sounder on-board the Ohzora (EXOS-C) and the Akebono (EXOS-D) satellites, *Adv. Space Res.*, doi:10.1016/j.asr.2006.10.019.

Whalen, J. A. (2004), Linear dependence of the postsunset equatorial anomaly electron density on solar flux and its relation to the maximum prereversal EXB drift velocity through its dependence on solar flux, *Journal of Geophysical Research (Space Physics)*, *109*(A18), doi:10.1029/2004JA010528.

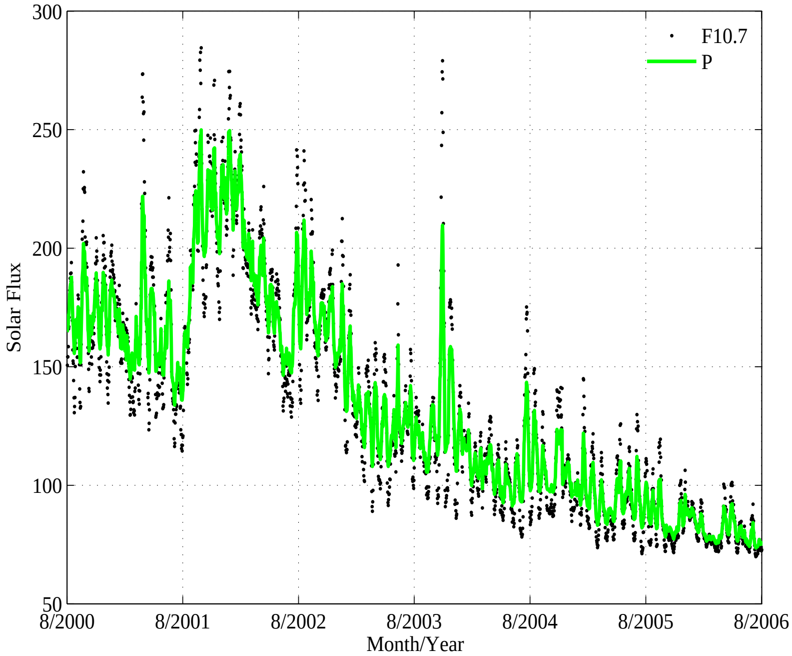

Figure 1. Values of F10.7 and P in unit of 10^{-22} W m^{-2} Hz^{-1} during the period of Aug. 1, 2000–Aug.1, 2006 which are used in this study.

Table 1. The Crest-to-Trough Ratio (CTR) near Equinoxes

	$P < 100$ (Low)	$100 \leq P \leq 150$ (Moderate)	$150 < P < 200$ (High)	$P \geq 200$ (Very high)
Noon	1.14	1.34	1.42	1.43
Post-sunset	1.30	1.47	3.9	29.17

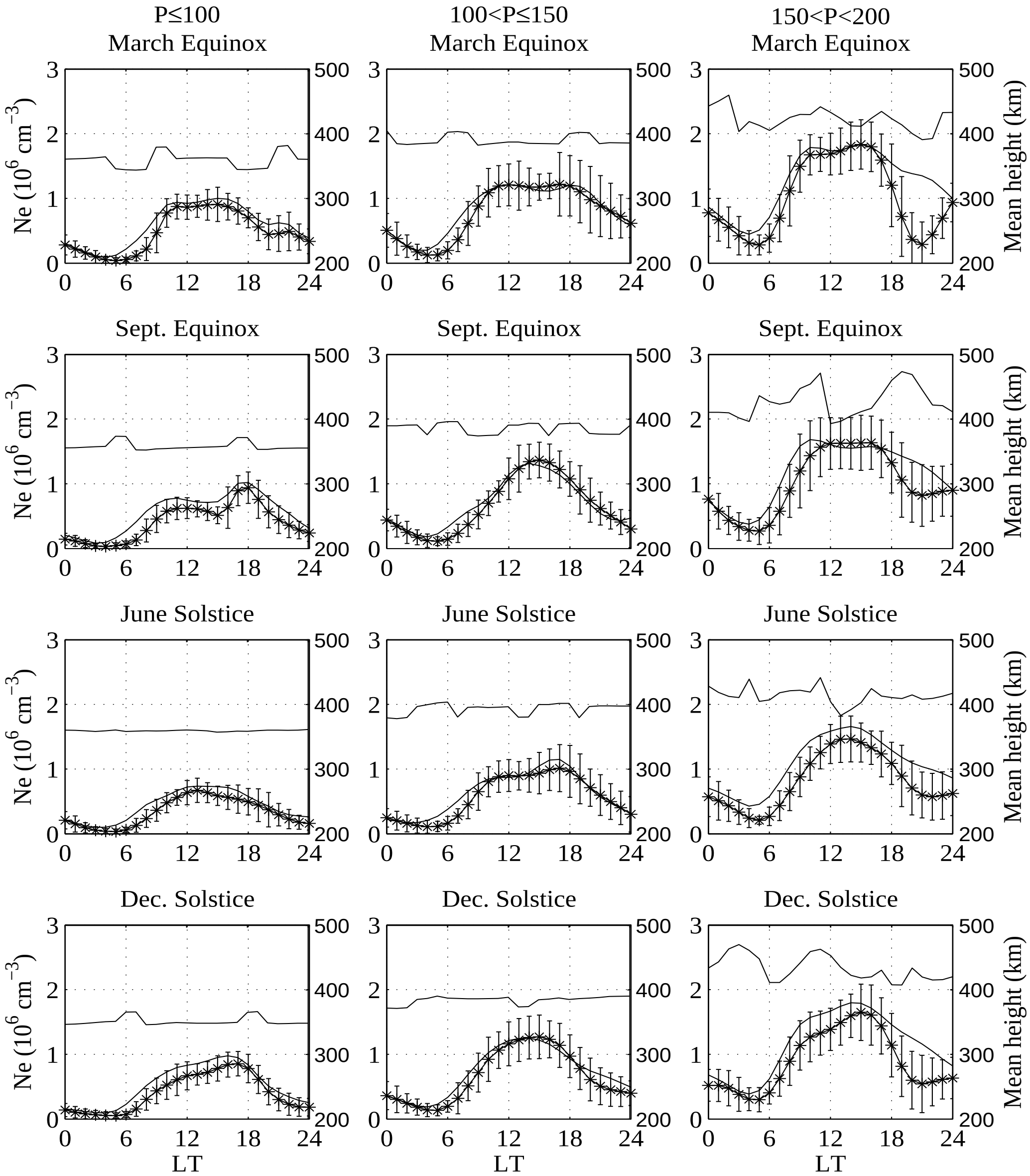

Figure 2. Diurnal variation of the electron density at the dip equator at 400 km obtained from CHAMP (star lines) and the IRI model (solid lines) at three solar flux levels. The error bars represent standard deviation. The average P values are about 85, 122, and 178. The mean satellite altitudes are given by the line in the upper part of each panel.

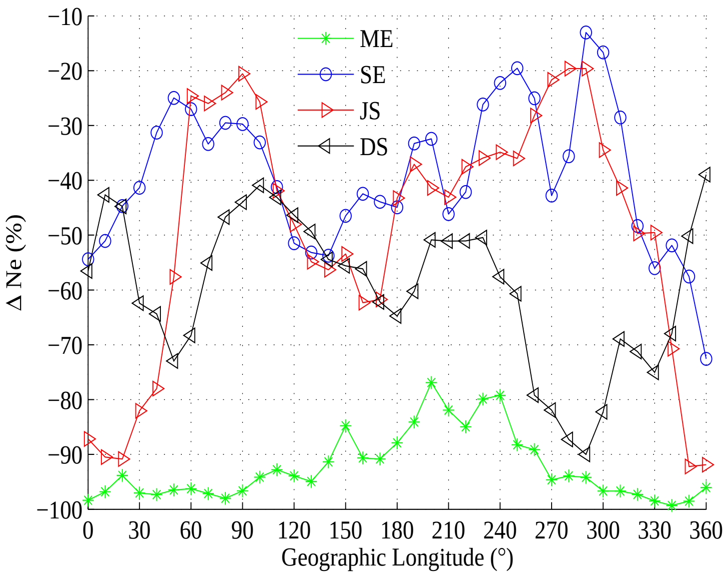

Figure 3. Longitudinal distribution of the percentage difference between the CHAMP and IRI electron density within 19–23 LT sector. The given seasons are the three-months periods centred at the equinox/solstice dates.

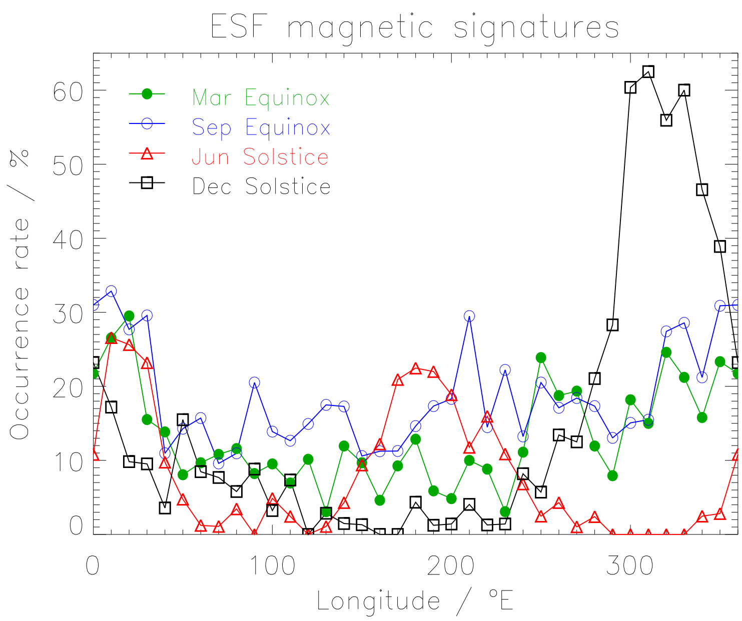

Figure 4. Longitudinal distribution of the occurrence rate of ESF magnetic signatures as observed by the CHAMP satellite for different seasons. The figure was adapted from Figure 5 in *Stolle et al.* [2006]. The given seasons are the three-months periods centred at the equinox/solstice dates.

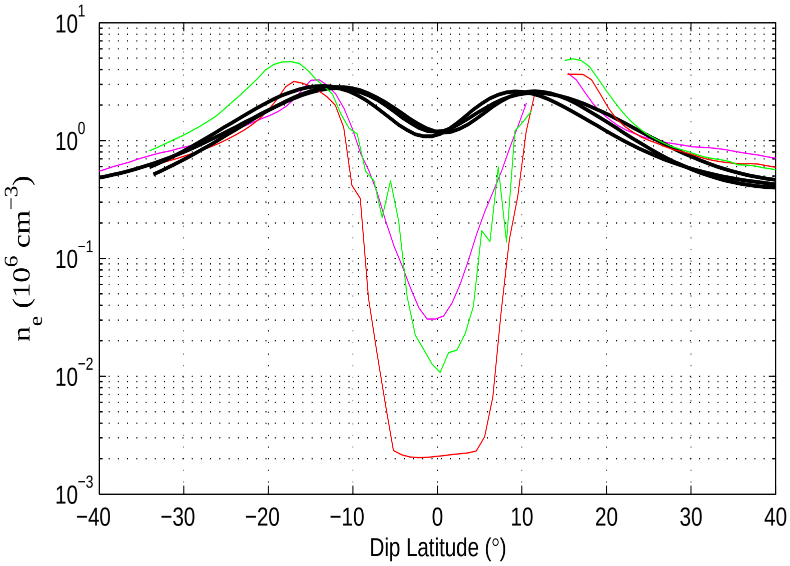

Figure 5. Several types of Ne latitudinal profiles seen in CHAMP satellite passes in comparison to those predicted by IRI2001. Since the PLP has a lower threshold of 2×10^3 cm^{-3}, the plateau in the red curve is an instrument effect and the real density could be even lower.

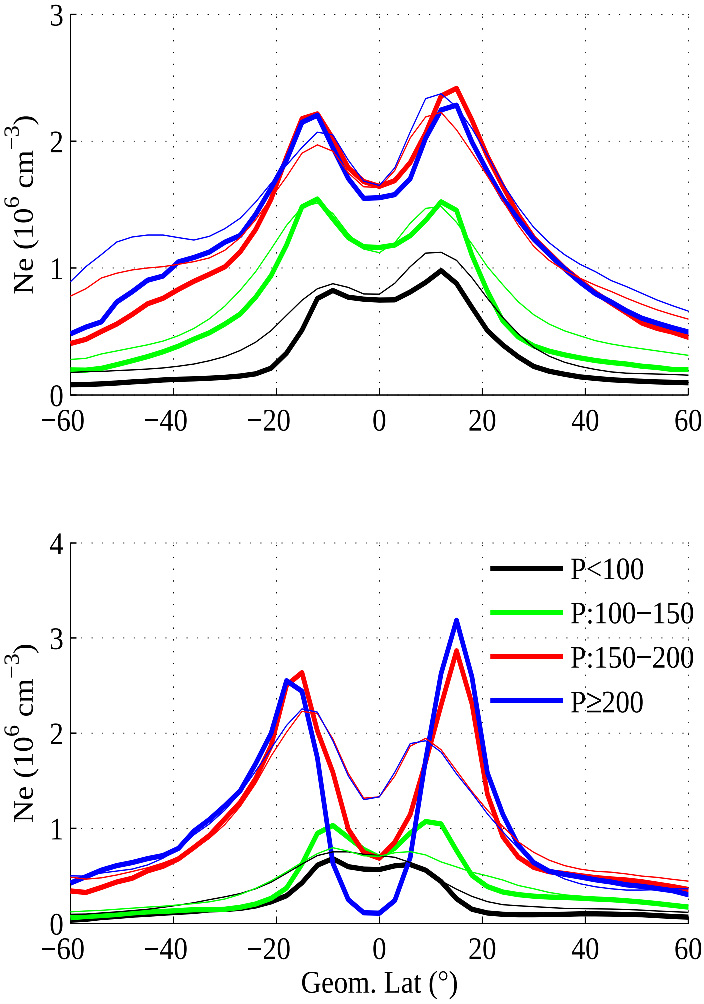

Figure 6. Quiet-time equinoxes (combined) Ne latitudinal distribution near 400 km altitude for various solar flux levels in noon (upper panel) and post-sunset (lower panel) local time sectors. Thick lines: CHAMP; thin lines: IRI. The mean P values are 81, 120, 177, and 217, respectively.

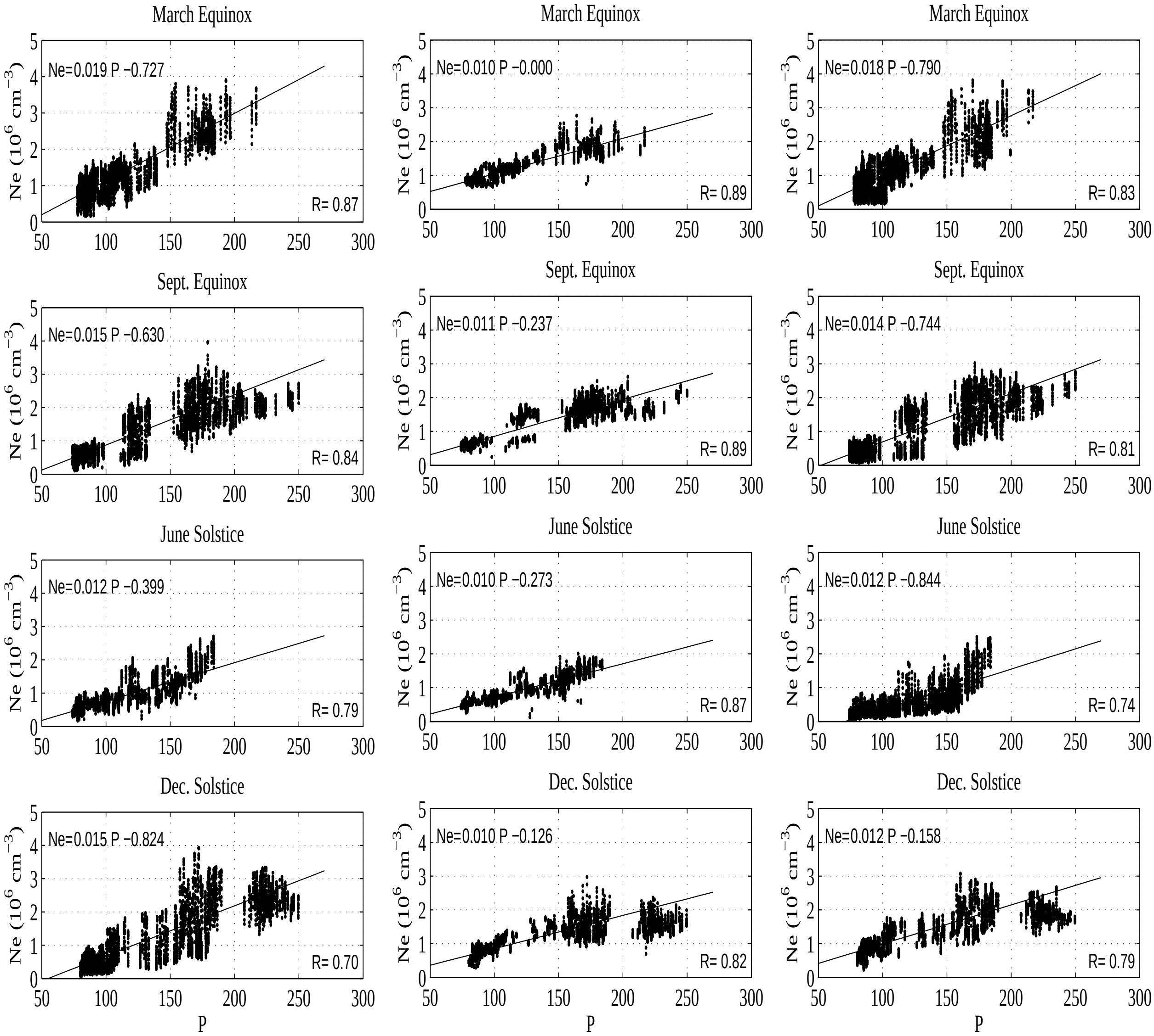

Figure 7. Solar activity (P) dependence of noon-time (11-15 MLT) Ne in different seasons for three latitude regions. Left column: the northern EIA crest; Middle column: the dip equator; Right column: the southern EIA crest. Data points at P>200 are not used in the fitting, hence has no influence on the slopes.

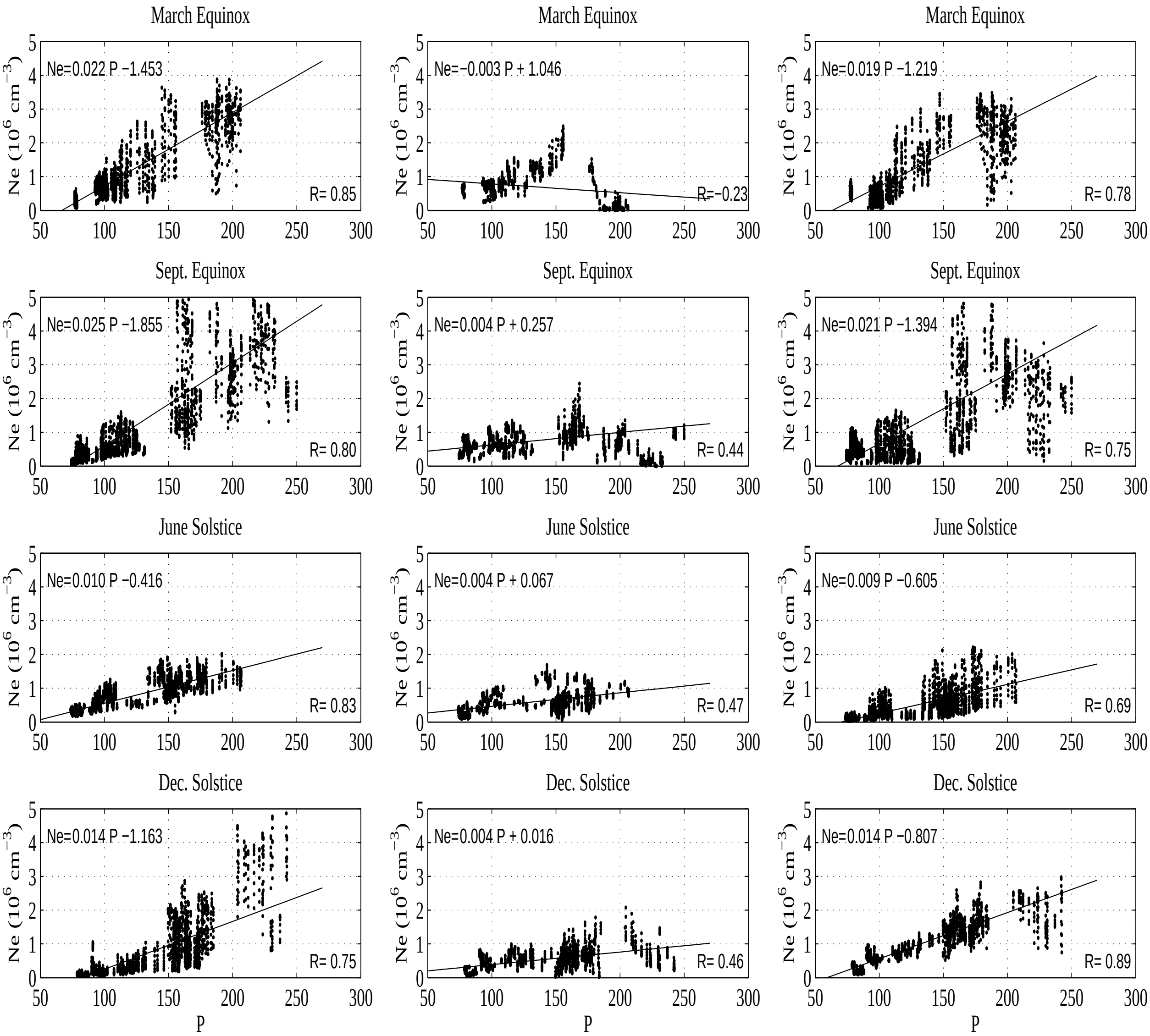

Figure 8. Same as Figure 7 but for post-sunset (18-23 MLT) sector. Left column: the northern EIA crest; Middle column: the dip equator; Right column: the southern EIA crest.

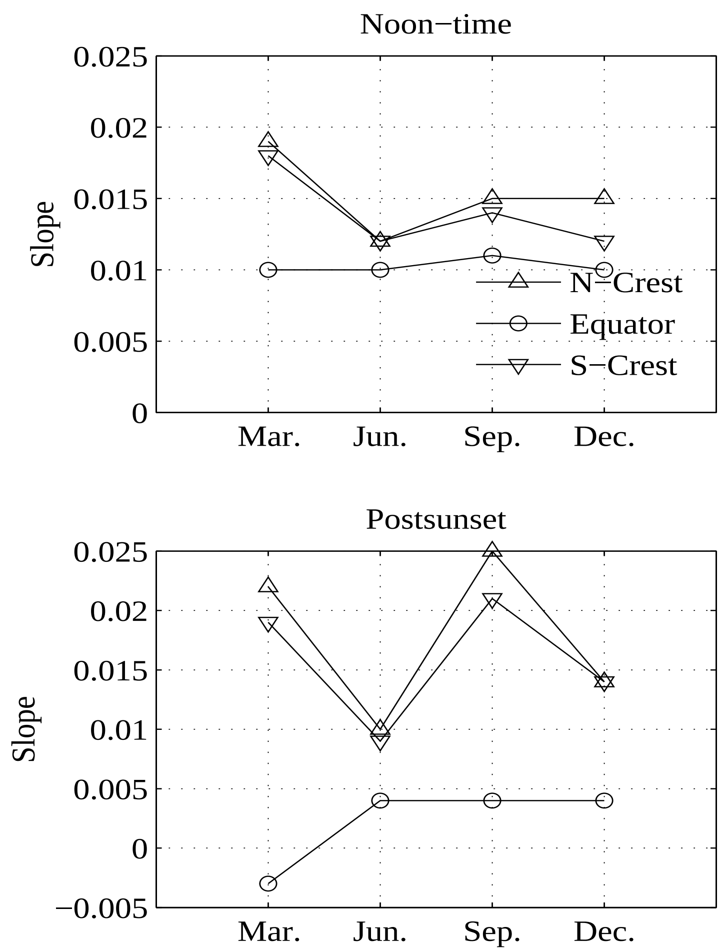

Figure 9. Slopes of the solar activity dependence of Ne in different seasons in the EIA trough and crest regions for noon and post-sunset local time sectors.

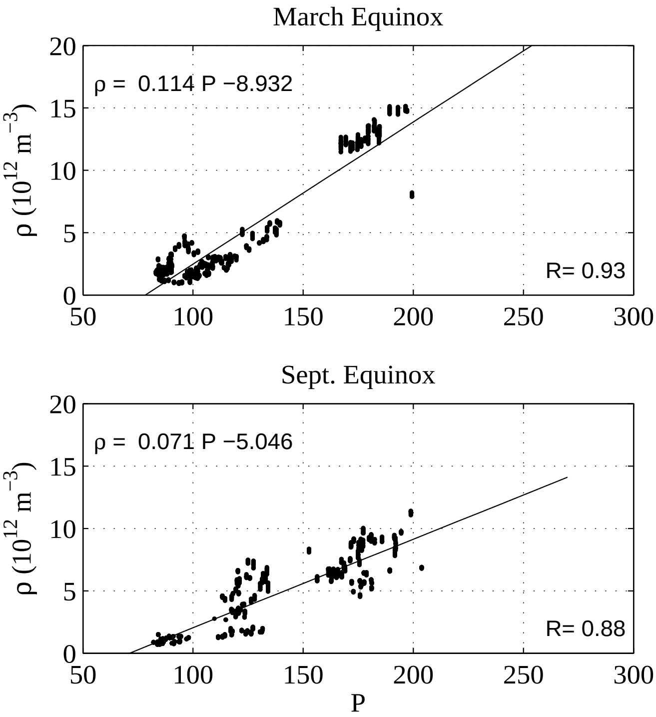

Figure 10. Solar activity dependence of the noontime neutral density at the dip equator.